Journal of Materials Chemistry A

PAPER

View Article Online
View Journal | View Issue



Cite this: J. Mater. Chem. A, 2016, 4, 6972

# Lithium-ion conductivity in $Li_6Y(BO_3)_3$: a thermally and electrochemically robust solid electrolyte†

Beatriz Lopez-Bermudez,[a] Wolfgang G. Zeier,[a] Shiliang Zhou,[a] Anna J. Lehner,[b] Jerry Hu,[b] David O. Scanlon,[cd] Benjamin J. Morgan*[e] and Brent C. Melot*[a]

Received 20th November 2015
Accepted 31st January 2016

DOI: 10.1039/c5ta09436d

www.rsc.org/MaterialsA

The development of new frameworks for solid electrolytes exhibiting fast Li-ion diffusion is critical for enabling new energy storage technologies. Here, we present a combined experimental and computational investigation into the ionic conductivity of $Li_6Y(BO_3)_3$, a new class of solid electrolytes with a pseudo-layered structure. Temperature-dependent impedance spectroscopy shows the pristine material exhibits an ionic conductivity of $2.2 \times 10^{-3}$ S cm$^{-1}$ around 400 °C, despite the fact that density functional theory calculations point to multiple remarkably low-energy diffusion pathways. Our calculations indicate small energy barriers for lithium interstitials to diffuse along one-dimensional channels oriented in the *c*-direction, and also for lithium vacancies diffusing within *ac* planes. This coexistence of diffusion mechanisms indicates that $Li_6Y(BO_3)_3$ is an extremely versatile host for exploring and understanding mechanisms for lithium-ion conductivity. We also find no evidence for reactivity with moisture in the atmosphere and that the material appears electrochemically stable when in direct contact with metallic lithium. This robust stability, alongside ionic conductivity that can be manipulated through appropriate aliovalent substitution, make $Li_6Y(BO_3)_3$ an exceptionally promising new class of solid electrolyte.

## 1 Introduction

Today, the most widely used lithium-ion electrolytes consist of fluorinated salts dissolved in non-aqueous organic solvents.[1] Setting aside safety and toxicity concerns, these salt solutions are incompatible with cell voltages above 5 V, which lies outside the window of electrochemical stability for these solvents.[2] Accordingly, there have been intense efforts to identify solid electrolytes with greater electrochemical stability, which would represent a critical step towards all-solid-state batteries with higher open-circuit voltages and improved safety characteristics.[3,4] To date, however, even the highest room-temperature ionic conductivities reported for solid electrolytes fall below those of commercial liquid electrolytes.[5] Furthermore, known solid lithium-ion electrolytes are often notoriously unstable under operating conditions.[6]

To be effective, solid electrolytes require high ionic conductivity, low electrical conductivity, and robust stability when in contact with alkaline metals like Li and Na.[7] Developing new materials that meet these criteria is particularly challenging. Known solid electrolytes typically belong to one of a few structural families, notably perovskite,[8–11] NASICON,[12–15] or garnet[16–21] lattices, which have all been heavily investigated over the years.

Here, we report the first observation of lithium-ion conductivity in $Li_6Y(BO_3)_3$, which is structurally distinct from all of the previously known solid electrolytes. This is not the first study on $Li_6Y(BO_3)_3$, but previous work has focused on the luminescent properties of rare-earth substituted compositions for use in lasers[22–31] and neutron scintillation detectors.[32,33] Although related borates like $Li_3BO_3$ and other ionically-conducting glasses have been studied,[34–37] to our knowledge, this is the first study of ionic transport properties of $Li_6Y(BO_3)_3$.

Using a combination of experimental and computational tools, we have investigated the nature of lithium transport through this new solid electrolyte. Temperature-dependent impedance spectroscopy on polycrystalline pellets shows an ionic conductivity of $2.2 \times 10^{-3}$ S cm$^{-1}$ near temperatures of 400 °C. Energy barriers for lithium-ion diffusion calculated using density functional theory show low-energy pathways for both lithium vacancies (0.23 eV) and lithium interstitials

[a]Department of Chemistry, University of Southern California, Los Angeles, CA 90089, USA. E-mail: melot@usc.edu

[b]Materials Research Laboratory, University of California, Santa Barbara, CA 93106, USA

[c]University College London, Kathleen Lonsdale Materials Chemistry, 20 Gordon Street, London WC1H 0AJ, UK

[d]Diamond Light Source Ltd., Diamond House, Harwell Science and Innovation Campus, Didcot, Oxfordshire OX11 0DE, UK

[e]Department of Chemistry, University of Bath, Claverton Down, BA2 7AY, UK

† Electronic supplementary information (ESI) available: The supporting information contains the thermal analysis data, scanning electron micrographs, and tables of the ionic conductivity and calculated vacancy formation energies of $Li_6Y(BO_3)_3$. See DOI: 10.1039/c5ta09436d

(0.20 eV), suggesting the potential for "bipolar" ionic conductivity, with the dominant conduction mechanism tunable through changes in sample stoichiometry. The presence of complex and numerous pathways for ionic conductivity in a robustly stable material makes $Li_6Y(BO_3)_3$ a promising new framework for the continued development of fast Li-ion conducting solid electrolytes.

# 2 Experimental

## 2.1 Synthesis

Polycrystalline samples of $Li_6Y(BO_3)_3$ were prepared *via* solid-state reactions using stoichiometric amounts of LiOH (Sigma Aldrich, ≥98%, powder), $Y_2O_3$ (Sigma Aldrich, 99.99%, powder) and $H_3BO_3$ (Sigma Aldrich, reagent grade plus ≥ 99.5%, powder). Prior to use, LiOH was dried at 300 °C for 24 h, and stored under vacuum. The starting materials were thoroughly ground for 30 min in an agate mortar, pressed into pellets using an isostatic press, and placed into a zirconia crucible. The resulting pellets were isolated from contact with the crucible using a small amount of powder with the same composition in order to avoid inadvertent contamination. The pellets were heated to 600 °C at 5 °C $min^{-1}$ in a tube furnace under flowing $N_2$ and held for 12 h to decompose the precursors. The pellets were subsequently ground, reformed into pellets, and heated to 600 °C at 5 °C $min^{-1}$ for 24 h, always under a stream of flowing $N_2$. This process was repeated three time to obtain phase pure materials according to standard laboratory X-ray diffraction. The use of $N_2$ atmosphere was found to be critical for obtaining phase-pure samples, as will be discussed.

## 2.2 Characterization

**2.2.1 X-ray diffraction.** Sample purity was evaluated using standard laboratory X-ray diffraction patterns, collected on a Bruker D8 diffractometer with a CoK$\alpha$ source ($\lambda_1 = 1.78897$ Å, $\lambda_2 = 1.79285$ Å), equipped with a LynxEye detector. Diffraction data were refined using the Rietveld method[38] as implemented in the FullProf suite of programs,[39] using the atomic coordinates determined by Péter *et al.* as a starting model.[30] Attempts were made to refine the structure of $Li_6Y(BO_3)_3$ against laboratory X-ray diffraction data starting from the positions determined using single crystal X-ray diffraction by Péter *et al.*;[30] however, due to the weak X-ray scattering form factors for the boron, oxygen and lithium, it was not possible to refine the atomic coordinates or thermal parameters.

**2.2.2 Thermal analysis.** Thermogravimetric analysis (TGA) and Differential Scanning Calorimetry (DSC) analyses were performed up to 500 °C using a platinum crucible in a simultaneous thermal analyser (Netzsch STA-449 Jupiter).

**2.2.3 Impedance spectroscopy.** Electrical transport measurements on polycrystalline pellets, with typical dimensions around 13 mm in diameter and 2 mm in thickness, were performed under $N_2$ between 25 °C and 450 °C. The density, determined from the geometry and mass of the pellets, is around ~70% of the theoretical density, indicating that the pellets are not fully densified. Attempts to increase the density were complicated by the tendency of the pellet to melt when heated at temperatures above 700 °C. Silver electrodes were applied using a thin layer of silver paste (SPI Conductive Silver Paste Plus) to ensure good coverage and were subsequently fired in air at 600 °C for 10 min to remove any trace organic from the colloidal suspension. Li electrodes were attached to the sample in an Ar-filled glove box by firmly pressing two disks of Li foil, 0.75 mm in thickness, on each face of the pellet. AC impedance spectroscopy was collected using an applied 200 mV sinus amplitude in the frequency range of 1 MHz to 100 mHz using a BioLogic VMP3 potentiostat.

**2.2.4 Microscopy.** Scanning Electron Microscopy (SEM) was performed on a JEOL JSM-7001 microscope (JEOL Ltd). The surface of a fractured pellet, shown in ESI Fig. S1,† indicated that the grains of the pellet were between 1–5 μm in diameter with good connectivity between each particle. No evidence for crystallite orientation was seen in the diffraction data or SEM images, so the experimental transport properties should be effectively isotropic and represent a scalar average of the tensor properties.

**2.2.5 Magic angle spinning nuclear magnetic resonance.** $^1H$, $^6Li$, and $^{11}B$ solid state Magic Angle Spinning Nuclear Magnetic Resonance (MAS NMR) spectroscopy measurements were performed at room temperature on a Bruker AVANCE III 800 MHz (18.8 T) standard bore spectrometer, operating at 800.1 MHz, 117.7 MHz, and 256.7 MHz for $^1H$, $^6Li$, and $^{11}B$, respectively. The chemical shifts were referenced as following: $^1H$: solid adamantane $C_{10}H_{16}$ ($\delta$ $^1H$: 1.71 ppm relative to TMS), $^6Li$: solid LiCl ($\delta$ $^6Li$: −0.85 ppm relative to 1 molar aqueous LiCl solution), $^{11}B$: cubic BN ($\delta$ $^{11}B$, 1.60 ppm relative to the diethylether borontrifluoride complex $BF_3 \cdot Et_2O$) All samples that were made under $N_2$ were handled in a $N_2$ glove box to evaluate the effect of moisture on the samples. Single pulse experiments for $^1H$ ($^{11}B$) were recorded with a $\pi/2$ ($\pi/12$) excitation pulse of 5 μs (0.62 μs) using a 10 s (60 s) relaxation delay, a 12.6 ms (13.1 ms) acquisition time, and an accumulation of 64 (16) scans in 2.5 mm zirconia rotor with a spinning rate of 30 kHz. The relaxation delay times were optimized for quantitative analysis. $^6Li$ $T_1$ longitudinal relaxation times were measured by the modified inversion-recovery method, where the single 180° pulse is replaced by a composite pulse for better inversion efficiency.[40] A range of 18 relaxation delay points between 1 ms and 3000 s with 8 scans per delay point was recorded for a sample packed into a 3.2 mm zirconia rotor spinning at 20 kHz. The relaxation data was fitted using the Bruker Dynamics Center software. A $^6Li$ 1D trace obtained by adding up the spectra for the longest three relaxation delay points, was deconvoluted by applying mixed Lorentzian/Gaussian line shapes using the Bruker Topspin software.

# 3 Theoretical methods

## 3.1 Density functional theory calculations

All density functional theory (DFT) calculations were performed using the VASP code.[41,42] Interactions between the core and valence electrons were described with the PAW method.[43] The calculations were performed using the PBEsol exchange–

correlation functional.[44] PBEsol is a revision of the PBE functional specifically tailored for solids, and yields structural data in excellent agreement with experiment. A planewave cutoff of 520 eV and a *k*-point sampling of 4 × 1 × 4 for the 76 atom unit cell of $Li_6Y(BO_3)_3$ were used, with the ionic forces converged to less than 0.01 eV $Å^{-1}$. Geometry optimized lithium vacancies, lithium interstitials, and Frenkel pairs were calculated in a 2 × 1 × 2 (304) atom supercell with a 2 × 2 × 2 Monkhorst–Pack special *k*-point grid, and all calculations were spin polarised.

### 3.2 Climbing nudged elastic band calculations

Diffusion barriers for lithium vacancies and interstitials were calculated using the climbing nudged elastic band (CNEB) method,[45] using the same 304 atom supercell as the geometry optimised defects, and only the *Γ*-point sampled. The end-point geometries were taken from the optimised defect structures. Each pathway was modeled using a minimum of three images (excluding the end-points), and was deemed to be converged when ionic forces on all images were less then 0.02 eV $Å^{-1}$.

## 4 Results

$Li_6Y(BO_3)_3$ crystallizes in a monoclinic space group and can be considered a polyanionic compound since all of the oxygen ions in the structure are part of $BO_3$ planar triangles (Fig. 1(a) and (b)). $YO_8$ dodecahedra share edges with each other to form chains that zig–zag along the *c*-axis, with $BO_3$ group fanning out perpendicular to the chain axis.

Stoichiometric $Li_6Y(BO_3)_3$ has six non-equivalent Li sites (see Fig. 2) in a dense and highly connected network. The layers containing the $YO_8$ chains are separated by planes of lithium. These Li-rich planes contain four distinct sites, denoted $Li^A$, $Li^B$, $Li^C$, and $Li^D$, are colored yellow in Fig. 1(a) and (b). Each of the sites within this layer adopt a highly distorted tetrahedral environment, whereas the two other sites, $Li^E$ and $Li^F$, are positioned between the $YO_8$ chains, to form an edge-sharing chain of $LiO_5$ trigonal bipyramids (see Fig. 2). All observed reflections could be indexed to the reported unit cell with no secondary reflections observed as seen in ESI Fig. S2.† Aside from the peak profile, only the lattice parameters could be accurately refined and were found to be $a = 7.182(2)$ Å, $b = 16.44(1)$ Å, $c = 6.641(5)$ Å and $\beta = 105.37(3)^\circ$, with $R_{Bragg} = 6.99\%$.

### 4.1 Ionic conductivity

AC impedance measurements were collected between temperatures of 25 °C and 450 °C under flowing nitrogen, with the results shown in Fig. 3(a). Prior to measuring the impedance, differential scanning calorimetry and thermal gravimetric analysis were performed up to 1100 °C in $N_2$, but showed no reactivity until the melting temperature of ~870 °C (ESI Fig. S3†). This implies the title phase is exceptionally stable to very high temperatures and does not exhibit any phase changes over the temperature interval of interest.

The ionic conductivity at room temperature was too low to measure; however, above 50 °C, impedance measurements

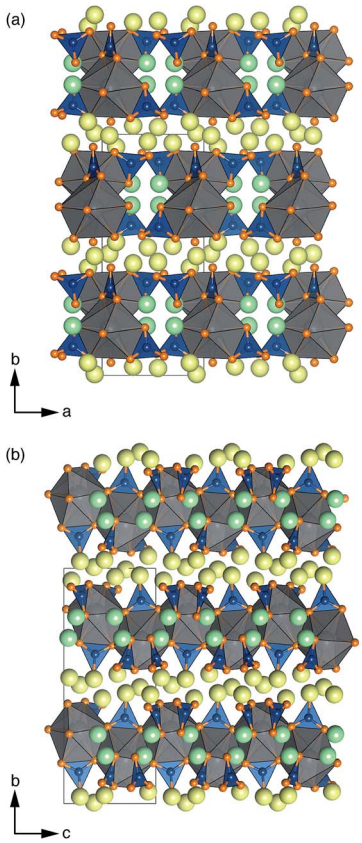


Fig. 1 Crystal structure of $Li_6Y(BO_3)_3$. Illustration of the crystal structure of monoclinic $Li_6Y(BO_3)_3$ viewed along the (a) *c*- and (b) *a*-axis. B is shown in blue, Y in gray, O in orange, and Li in yellow or green. Edge-sharing $YO_8$ dodecahedra form chains that zig–zag along the *c*-axis. Trigonal bipyramidal chains of $LiO_5$ form along the *c*-direction and connect the chains of $YO_8$ along the *a*-direction.

using Ag electrodes reveal a single semicircle with a linear tail, as expected when the motion of Li-ions through the pellet is blocked at the interface of the silver electrode (Fig. 3(b)). Replacing silver with a non-blocking lithium foil, shown in Fig. 3(c), causes the tail to disappear, confirming its association with the diffusion of lithium through the pellet. Conductivity measurements using Li electrodes could only be collected to 150 °C due to the low melting point of metallic Li.

After heating, the Li electrodes were removed and no sign of discoloration could be seen on the pellet. To further test the stability of the phase when in contact with Li, a pellet was wrapped in Li foil, placed in a carbon-coated fused silica tube and heated to 300 °C for several hours. After gently peeling away the resulting ingot of Li, the pristine white pellet was recovered, demonstrating a very robust stability when in direct contact with metallic Li foil.

The single semicircle in the impedance data was fit using an equivalent circuit consisting of a resistor in series with two parallel CPE/resistor components; a model meant to take into account the contact resistance of the silver (or Li) in series with ionic conductivity through the bulk and grain boundaries of the pellet. Despite the significantly increased temperature, no contribution from electrical conductivity was detected, with the

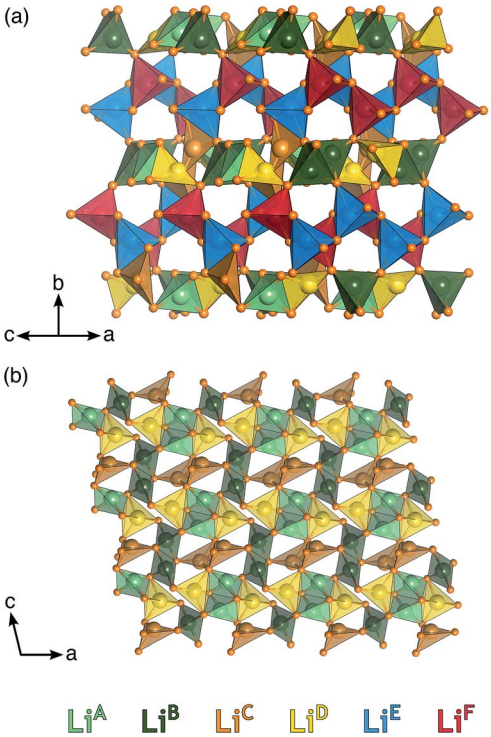


Fig. 2 Local coordination environment of each Li site in $Li_6Y(BO_3)_3$. Illustration of the polyhedral connectivity between the six neighboring Li positions viewed along the (a) [101] and (b) [010] unit cell directions. There are two distinct topologies in the structure: the edge sharing ribbons of $Li^E$ and $Li^F$ and the layers of $Li^{A-D}$. For clarity, Y and B are not shown.

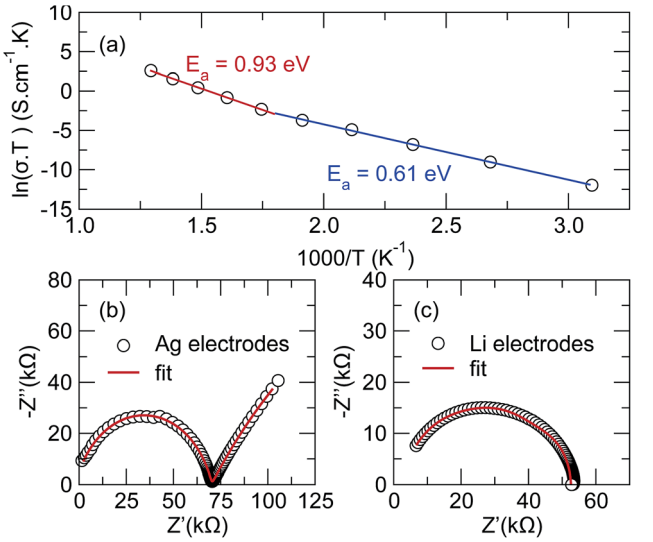


Fig. 3 Temperature-dependent ionic conductivity with Li and Ag electrodes. (a) Arrhenius plot for the total lithium ion conductivity of $Li_6Y(BO_3)_3$ as a function of temperature using Ag electrodes. An activation energy 0.61 eV is found by fitting data up to 350 °C, while an activation energy 0.93 eV is found when the data between 350 °C and 500 °C is fit. AC impedance obtained at 150 °C, using Ag electrodes (b) and Li electrodes (c). The minimum (maximum) frequency depicted for (b) and (c) are 192 mHz (614 kHz) and 1 Hz (1 MHz) respectively. The disappearance of the tail at low frequencies when using reversible Li electrodes confirms the blocking of mobile Li ions by the Ag. The red line shows fits to equivalent circuit discussed in the text.

dc resistance of the pellet remaining outside the range of the voltmeter, suggesting it to be several MΩ at minimum. It should be noted that the data in Fig. 3(b) fails to pass through the origin because of the high frequency limit of the potentiostat and that since the pellet is not fully dense, the individual arcs associated with the grain boundary and bulk transport cannot be fully resolved. For this reason, the reported conductivity values should be taken as a lower estimate for the true bulk conductivity of the material.[46] A table of the ionic conductivity values at each temperature is given in ESI Table S1.†

The temperature-dependent ionic conductivity, shown in Fig. 3(a), increases from $1.9 \times 10^{-8}$ S cm$^{-1}$ at 50 °C to $2.2 \times 10^{-3}$ S cm$^{-1}$ by 400 °C, indicating good ionic conductivities at higher temperatures. Two regions with distinctly different slopes can be see, with a crossover occurring around 300 °C. Fitting the interval between 50 °C and 300 °C to an Arrhenius expression gives an activation energy of $E_a = 0.61$ eV while fitting from 350 °C and 500 °C indicates an activation energy of $E_a = 0.93$ eV. The observation of two distinct linear regions in the Arrhenius plot is not uncommon, and generally indicates competition between two or more diffusion mechanisms.[47]

### 4.2 MAS NMR spectroscopy

MAS NMR experiments were performed to examine the local environments of lithium in the samples. We first collected $^1$H NMR data, which are shown on the left hand side of ESI Fig. S4.† No obvious differences were found between the empty rotor and samples made or stored in air for several weeks, showing no significant exchange of $Li^+$ for $H^+$ after synthesis. There is also no evidence that preparing the phase in air *versus* dry $N_2$ results in proton substitution into the bulk. This stability with respect to proton exchange contrasts with Li-conducting garnets, such as $Li_6BaLa_2Ta_2O_{12}$, where rapid proton exchange can degrade the material's performance over time.[21]

The right-hand side of ESI Fig. S4† shows signals between 15 and 20 ppm in the $^{11}$B spectra corresponding to the three crystallographic sites; broad as expected for boron in trigonal-planar coordination. A sharp signal close to 1 ppm, with an area of roughly 10%, seems to indicate a boron-containing impurity is present in samples that were prepared in open air. While the composition of this impurity can not be directly determined, preparing the materials under dry flowing $N_2$ appears to suppress this signal, which suggests this is most likely the result of a deleterious reaction of LiOH or $H_3BO_3$ with moisture in the atmosphere. Most importantly, once formed we find no evidence for proton exchange with the atmosphere in these materials.

Due to broadening effects of homonuclear dipolar coupling and the second-order quadrupolar interaction in $^7$Li NMR, the $^7$Li NMR spectrum contains only a single unresolved peak, which corresponds to a number of unique Li sites and coordination environments.[48] Higher resolution spectra are possible for $^6$Li, due to the narrower line widths of the center band

resonances that result from weaker quadrupolar and homonuclear dipolar coupling interactions of $^{6}$Li compared to $^{7}$Li. To improve the resolution further, we conducted a series of $^{6}$Li inversion-recovery experiments, which allow the resolution of signals as a function of the spin–lattice relaxation time, $T_1$. The $^{6}$Li $T_1$ data, shown as a pseudo-2D NMR contour plot in the bottom part of Fig. 4(a), reveal at least six different components, corresponding to distinct Li sites or groups of sites with similar spin–lattice relaxation behavior at room temperature. The $T_1$ times for those components range from 850 to 2200 s, with the slowest spin-relaxation processes observed for the Li nuclei associated with the chemical shifts at the edges of the overlapping $^{6}$Li spectral feature at 0.2 and 1.3 ppm, respectively. The 1D trace projected on the top panel was derived by adding up the spectra of the three inversion-recovery experiments with the longest relaxation delay times and can be considered an adequate representation of a single pulse experiment with the required long relaxation delay.

Based on the $T_1$ resolved results, this trace was deconvoluted with a good fit into six spectral components. A static picture of the crystal structure would suggest that lithium occupies each of the six distinct crystallographic sites, $Li^{\{A-F\}}$, in equal proportion. The integrated areas for the six components of the $^{6}$Li spectrum, however, are not all equal, but instead show relative populations from 1 to 0.09. Fitting with more equal-ratio spectral components would require deconvolution into at least nine functions, with multiple sites being concentrated around the extremes of the chemical shift range. We interpret this population inhomogeneity as indicating lithium-exchange between different sites on an NMR timescale, and can speculate that the signals at the edges of broad feature in the 1D trace correspond to collections of highly similar lithium environments that are preferentially occupied by lithium.

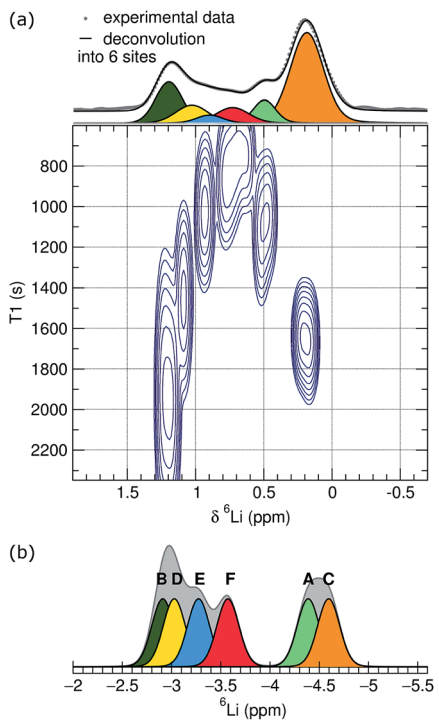


Fig. 4 Experimental and simulated NMR patterns. (a) $^{6}$Li NMR results for $Li_6Y(BO_3)_3$. The contour plot shows the results of the inversion-recovery experiments indicating at least six different Li species. The projection on top represents the added traces of the longest relaxation delay spectra and a fit as a deconvolution into six spectral components. (b) Simulated $^{6}$Li spectrum of $Li_6Y(BO_3)_3$ using the DFT chemical shift values for the six crystallographic Li sites and arbitrary Gaussian line shapes.

To help assign these NMR data, we used density functional theory (DFT) to calculate Li chemical shifts for each of the six crystallographic sites in the perfect $Li_6Y(BO_3)_3$ structure, which were then used to construct a simple simulated $^{6}$Li spectrum by convoluting with a Gaussian line shape (Fig. 4(b)). It is important to keep in mind that $T_1$ relaxation is a complex phenomenon that can not yet be accurately simulated, and a quantitative comparison of the DFT simulations and the experimental $T_1$ NMR results is not possible. The shape and width of the simulated spectrum, however, do agree well with the experimental results. Although the calculated chemical shifts are systematically moved upfield by approximately 5 ppm, the calculated chemical shift *differences* are in good qualitative agreement with the observed distribution of maxima in the pseudo-2D spectrum.

Comparing the experimental and simulated $^{6}$Li NMR data, the fastest $T_1$ times can be assigned to the $Li^{E}$ and $Li^{F}$ sites—the two sites located in the chains found in the same plane as the $YO_8$ and $BO_3$ groups—and the longer $T_1$ times assigned to sites $Li^{A-D}$—located in the Li-rich layers of the crystal structure.

### 4.3 Computational Li-diffusion profiles

The presence of multiple non-equivalent Li sites in $Li_6Y(BO_3)_3$ makes a mechanistic description of lithium-ion transport a particular challenge. To better understand the role of lithium disorder and diffusion by competing pathways, we performed DFT calculations on lithium interstitials, vacancies, and Frenkel pairs, and calculated potential energy barriers for lithium vacancy and interstitial point defect diffusion.

### 4.4 Lithium defect energies

We first calculated relative energies for lithium vacancies at each of the six non-equivalent lithium sites. The calculated vacancy formation energies are listed in ESI Table S2.† The preferred vacancy position is site $Li^{A}$, with a vacancy formation energy of 4.09 eV (relative to metallic Li). Relative to the $Li^{A}$ site, vacancies at the other three sites in the Li-rich *ac* planes ($Li^{B-D}$) are higher in energy by between 0.18 eV and 0.42 eV. In contrast, vacancy energies at $Li^{E}$ and $Li^{F}$ (those lithium sites in the 1D *c* chains) are higher than $Li^{A}$ by 0.62 eV and 0.70 eV respectively. Li vacancies, therefore, preferentially occupy the dense Li-rich $Li^{A-D}$ planes, which can be explained by the expected large reduction in Li–Li repulsion. The relatively low lithium ion density between the $YO_8$ chains means interstitial lithium can be accommodated in between the $Li^{E}$ and $Li^{F}$ sites. The formation energy for interstitials at this site, relative to metallic Li, is 1.44 eV. The Frenkel pair formation energy was calculated as the difference in energy between a perfect stoichiometric

 

system, and a Frenkel-pair-defective system with a vacancy at $Li^A$ (the lowest energy vacancy site) and an interstitial at a non-adjacent interstitial site. This gave a formation energy of 0.81 eV (Fig. 5).

### 4.5 Lithium diffusion barriers

To identify preferred diffusion pathways for lithium vacancies we considered potential paths between all lithium-site pairs with separations ≤4 Å (15 paths in total), and calculated barriers using the CNEB approach. These calculated diffusion barriers are shown schematically in Fig. 6.

The lowest energy diffusion pathway for Li vacancy hopping is *via* $Li^A \rightarrow Li^B \rightarrow Li^B \rightarrow Li^A$, which has a maximum barrier height of 0.23 eV. Vacancy diffusion *via* $Li^A \rightarrow Li^C \rightarrow Li^A \rightarrow Li^A$ has a slightly higher maximum barrier height of 0.34 eV. Lithium-vacancy transport along the *b* direction requires involvement of the $Li^E$ and $Li^F$ sites. These sites have the highest vacancy energies, and are also associated with large vacancy diffusion barriers. The lowest-energy vacancy-hopping process along *b* proceeds *via* $Li^C \rightarrow Li^E \rightarrow Li^F \rightarrow Li^D \rightarrow Li^C$, and has a maximum barrier of 0.97 eV. The high vacancy diffusion barriers for transport along *b* means lithium-vacancy transport is effectively restricted to a 2D process within the Li-rich *ac* planes.

For lithium interstitial transport, the *c*-aligned chains of $YO_8$ polyhedra block direct diffusion along *a*. We therefore only consider transport along *b* and *c*; in each case calculating CNEB barriers for *interstitialcy* mechanisms along these directions. The first considered interstitialcy mechanism involved only the $Li^E/Li^F$ sites and corresponds to one-dimensional transport along the *c*-oriented channels. Instead of jumping directly to a neighbouring interstitial site, interstitial Li displaces a neighbouring lithium ion at either a $Li^E$ or $Li^F$ site, and this second moves to occupy the adjacent interstitial site. In the second considered interstitialcy mechanism, the interstitial lithium moves along *b* into the Li-rich *ac* plane, displacing the closest $Li^B$ ion. This second ion moves to the adjacent $Li^B$ site, displacing a third ion that moves along *b* to a new interstitial site. The CNEB calculated barriers for these two mechanisms are 0.20 eV for *c*-channel diffusion involving exchange with the $Li^F$ site (0.26 eV *via* the $Li^E$ site), and 0.80 eV for diffusion along *b*. This indicates interstitials can undergo rapid one-dimensional transport along the $Li^E/Li^F$ channels aligned along *c*, whereas interstitial transport through the Li-rich $Li^{A–D}$ planes (which is necessary for transport along *b* or indirect transport along *a*) is much less effective. We attribute this highly anisotropic behaviour to a large energy penalty associated with disrupting the dense lithium packing in the $Li^{A–D}$ plane.

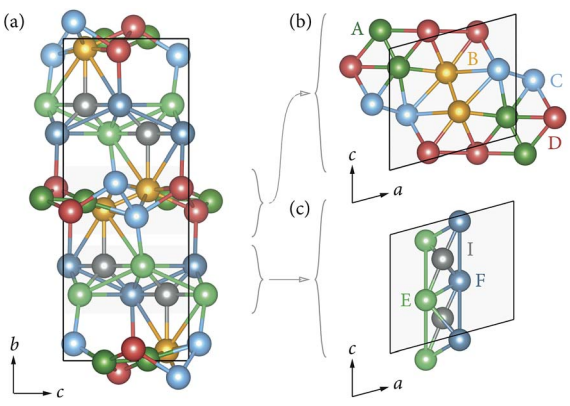


Fig. 5 Illustration of the Li sites with respect to each other. Illustration of the various Li positions with respect to each other viewed down the (a) *c*-axis, (b) with the Li-rich layer, and (c) within the 1D chains.

The calculated point-defect diffusion barriers reveal low energy pathways of 0.23 eV and 0.20 eV respectively for both lithium vacancies and interstitials. This suggests $Li_6Y(BO_3)_3$ may exhibit "bipolar" ionic conductivity, where the dominant lithium-transport process depends on the precise defect stoichiometry of the samples. Interestingly, interstitial and vacancy diffusion are both predicted to be highly anisotropic, and also to preferentially occur in *different* regions of the crystal lattice. Vacancy diffusion is favored along *a* and *c* directions within the $Li^{A–D}$ layers, but again disfavored along *b*, because of the high vacancy energies for the $Li^E/Li^F$ sites. Interstitial diffusion, in contrast, is favored along the $Li^E/Li^F$ chains oriented along the *c*-axis, but disfavored along *b*, which involves disruption of the $Li^{A–D}$ layers (and effectively blocked along *a* by the $YO_8$ chains).

## 5 Discussion

Our DFT calculations reveal extremely low barriers for lithium interstitial and vacancy diffusion (0.20 eV and 0.23 eV respectively). In highly stoichiometric samples, however, *intrinsic* concentrations of lithium interstitial or vacancy defects are small, and lithium conduction at even moderate temperatures requires thermal formation of Frenkel pairs. In this case measured conduction activation energies will depend on both the Frenkel pair formation energy and the hopping energy of the most mobile defect, *via*

$$\Delta E_a = \Delta E_{hop}^{defect} + \frac{\Delta E_{FP}}{2}, \quad (1)$$

where $\Delta E_{hop}^{defect}$ is the barrier to diffusion by a specific defect, and $\Delta E_{FP}$ is the Frenkel pair formation energy. Using the calculated Li interstitial diffusion barrier of 0.20 eV and Frenkel pair formation energy of 0.81 eV, this predicts an intrinsic activation energy of 0.61 eV. This agrees extremely well with the experimental activation energy from our ac-impedance data of 0.61 eV at temperatures below 325 °C. We therefore predict that lithium transport in as-formed $Li_6Y(BO_3)_3$ is dependent on intrinsic Frenkel pair formation and subsequent diffusion of lithium interstitials and vacancies. The lower calculated diffusion barrier for lithium interstitials compared to vacancies suggests that interstitialcy transport along the *c* channels is the dominant conduction mechanism in the stoichiometric material. Because the calculated diffusion barrier for vacancy diffusion is only 0.03 eV higher both interstitial and vacancy diffusion are expected to contribute to lithium conduction.

Above 325 °C the observed activation energy increases to 0.93 eV. This can be explained either by competing diffusion

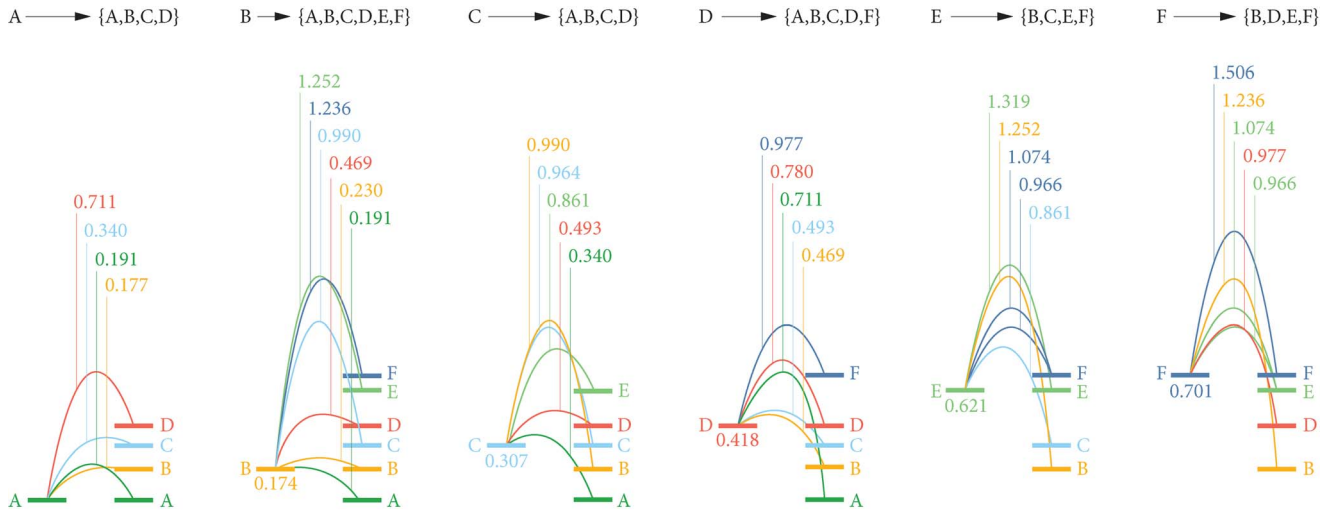


Fig. 6 Calculated energy barriers for vacancy diffusion between each site. Schematic of the calculated minimum energy barriers for all Li–Li site vacancy hops with site separations ≤4 Å. All energies are in eV, and give the maximum energy along each minimum-energy path relative to the energy of a vacancy at site $Li^{A}$. Relative energies of vacancies at sites $Li^{\{B-F\}}$ are also given.

mechanisms, or competing defect formation processes, which start to contribute to net ionic conduction at these elevated temperatures. In the latter case, the increase in activation energy is consistent with Frenkel pair formation with vacancies at sites $Li^{E}/Li^{F}$, which would increase the total number of interstitials available to conduct along the *c* channels, and corresponds to a predicted activation energy of 0.92 eV.

The relatively high activation energy of 0.61 eV in the low-temperature regime means that not enough carriers are mobile enough to measure the ionic conductivity of pristine $Li_6Y(BO_3)_3$ at room temperature. It should be emphasised, however, that this is the case for the formally stoichiometric material, and our calculated defect energies and diffusion barriers support the model that in this pristine material lithium-ion conduction is dependent on *intrinsic* Frenkel pair formation. The relatively low calculated barriers of 0.20 eV for lithium interstitial transport along *c*, and 0.23 eV for lithium vacancy transport in the *ac* plane suggest that non-stoichiometric forms should exhibit significantly higher *extrinsic* ionic conductivity. Indeed, controlling lithium stoichiometry through aliovalent substitutions is a straightforward route to enhanced ionic conductivities in other solid lithium-electrolytes.[8] Notably, the calculated barriers for both vacancy and interstitial transport in $Li_6Y(BO_3)_3$ are lower than for the "best in class" Li-garnet of 0.35 eV.[7] The existence of low energy defect diffusion pathways for both interstitials and vacancies suggests both sub- and supervalent doping strategies might produce high room-temperature ionic conductivities. Coupled with the spatially distinct regions for interstitial *versus* vacancy diffusion (*via* 1D *c* channels for interstitials, and 2D *ac* layers for vacancies) $Li_6Y(BO_3)_3$ presents a particularly versatile host framework for exploring lithium-ion conductivity. Combined with exceptional electrochemical stability with respect to moisture and under high voltages, $Li_6Y(BO_3)_3$ is a highly promising new framework for the future development of new solid electrolytes that exhibit fast ionic conductivity that could be tuned at the synthetic level.

## 6 Conclusions

In summary, we have characterized the temperature-dependent Li-ion conductivity of $Li_6Y(BO_3)_3$ using an array of experimental and computational tools. While the ionic conductivity does not reach $2.2 \times 10^{-3}$ S cm$^{-1}$ until temperatures as high as 400 °C, the thermal and electrochemical stability of the pristine phase offers the promise of an exceptionally robust solid electrolyte if the ionic conductivity at room temperature can be enhanced. Defect formation energies and lithium-ion diffusion barriers calculated using density functional theory calculations support the model that in the pristine stoichiometric material lithium conductivity is limited by Frenkel pair formation, but that greatly improved ionic conductivities associated with activation energies as low as 0.20 eV could achieved through appropriate aliovalent chemical substitution to achieve Li-ion non-stoichiometry. Thus, proper modifications to the pristine $Li_6Y(BO_3)_3$ should serve as a promising new platform for the development of high performance solid electrolytes.

## Acknowledgements

B. C. M., B. A. L. B., W. G. Z., and S. Z. gratefully acknowledge financial support through start-up funding provided by the Dana and David Dornsife College of Letters and Sciences at the University of Southern California. A. J. L. gratefully acknowledges support of Swiss National Science Foundation fellowship number PBSKP2-145825. W. G. Z. also acknowledges the support by a fellowship within the Postdoc-Program of the German Academic Exchange Service (DAAD). B. J. M. acknowledges support from the Royal Society (UF130329). D. O. S. acknowledges support from EPSRC (EP/N001982/1). The

computational work presented here made use of the ARCHER supercomputer through our membership of the UK's HPC Materials Chemistry Consortium, which is funded by EPSRC grant EP/L000202. The authors also acknowledge use of the MRL facilities at UCSB, part of the MRSEC Program of the NSF under Award No. DMR 1121053; a member of the NSF-funded Materials Research Facilities Network.

## References

1 J.-M. Tarascon and M. Armand, *Nature*, 2001, **414**, 359–367.
2 K. Xu, *Chem. Rev.*, 2014, **114**, 11503–11618.
3 J. B. Goodenough and K.-S. Park, *J. Am. Chem. Soc.*, 2013, **135**, 1167–1176.
4 Y. Shao, F. Ding, J. Xiao, J. Zhang, W. Xu, S. Park, J.-G. Zhang, Y. Wang and J. Liu, *Adv. Funct. Mater.*, 2013, **23**, 987–1004.
5 N. Kamaya, K. Homma, Y. Yamakawa, M. Hirayama, R. Kanno, M. Yonemura, T. Kamiyama, Y. Kato, S. Hama, K. Kawamoto and A. Mitsui, *Nat. Mater.*, 2011, **10**, 682–686.
6 L. Truong, S. Narayanana and V. Thangadurai, *ECS Trans.*, 2013, **45**, 21–29.
7 V. Thangadurai and W. Weppner, *Ionics*, 2006, **12**, 81–92.
8 S. Stramare, V. Thangadurai and W. Weppner, *Chem. Mater.*, 2003, **15**, 3974–3990.
9 P. Birke, S. Scharner, R. A. Huggins and W. Weppner, *J. Electrochem. Soc.*, 1997, **144**, L167–L169.
10 Y. Inaguma, C. Liquan, M. Itoh, T. Nakamura, T. Uchida, H. Ikuta and M. Wakihara, *Solid State Commun.*, 1993, **86**, 689–693.
11 E. E. Jay, M. J. D. Rushton, A. Chroneos, R. W. Grimes and J. A. Kilner, *Phys. Chem. Chem. Phys.*, 2015, **17**, 178–183.
12 H. Aono, E. Sugimoto, Y. Sadaoka, N. Imanaka and G. Adachi, *J. Electrochem. Soc.*, 1989, **136**, 590–591.
13 H. Aono, E. Sugimoto, Y. Sadaoka, N. Imanaka and G. Adachi, *J. Electrochem. Soc.*, 1990, **137**, 1023–1027.
14 B. Wang, M. Greenblatt, S. Wang and S. J. Hwu, *Chem. Mater.*, 1993, **5**, 23–26.
15 Z. Liu, S. Venkatachalam and L. van Wüllen, *Solid State Ionics*, 2015, **276**, 47–55.
16 R. Murugan, V. Thangadurai and W. Weppner, *Angew. Chem., Int. Ed.*, 2007, **46**, 7778–7781.
17 E. J. Cussen, T. W. S. Yip, G. O'Neill and M. P. O'Callaghan, *J. Solid State Chem.*, 2011, **184**, 470–475.
18 E. J. Cussen, *J. Mater. Chem.*, 2010, **20**, 5167–5173.
19 Y. Li, J.-T. Han, C.-A. Wang, H. Xie and J. B. Goodenough, *J. Mater. Chem.*, 2012, **22**, 15357–15361.
20 J. Han, J. Zhu, Y. Li, X. Yu, S. Wang, G. Wu, H. Xie, S. C. Vogel, F. Izumi, K. Momma, Y. Kawamura, Y. Huang, J. B. Goodenough and Y. Zhao, *Chem. Commun.*, 2012, **48**, 9840–9842.
21 W. G. Zeier, S. Zhou, B. Lopez-Bermudez, K. Page and B. C. Melot, *ACS Appl. Mater. Interfaces*, 2014, **6**, 10900–10907.
22 A. R. Devi and C. K. Jayasankar, *Mater. Chem. Phys.*, 1995, **42**, 106–119.
23 V. Jubera, J. P. Chaminade, A. Garcia, F. Guillen and C. Fouassier, *J. Lumin.*, 2003, **101**, 1–10.
24 E. F. Dolzhenkova, V. N. Baumer and A. V. Tolmachev, *Crystallogr. Rep.*, 2005, **50**, 1060–1064.
25 R. P. Yavetski, E. F. Dolzhenkova, M. F. Dubovik, T. I. Korshikova and A. V. Tolmachev, *Crystallogr. Rep.*, 2005, **50**, S88–S91.
26 J. Sablayrolles, V. Jubera, J.-P. Chaminade, I. Manek-Hönninger, S. Murugan, T. Cardinal, R. Olazcuaga, A. Garcia and F. Salin, *Opt. Mater.*, 2005, **27**, 1681–1685.
27 J. Sablayrolles, V. Jubera, F. Guillen, R. Decourt, M. Couzi, J. Chaminade and A. Garcia, *Opt. Commun.*, 2007, **280**, 103–109.
28 J. Sablayrolles, V. Jubera, M. Delaigue, I. Manek-Hönninger, J.-P. Chaminade, J. Hejtmanek, R. Decourt and A. Garcia, *Mater. Chem. Phys.*, 2009, **115**, 512–515.
29 I. N. Ogorodnikov, I. N. Sedunova, A. V. Tolmachev and R. P. Yavetskiy, *Opt. Spectrosc.*, 2012, **113**, 66–72.
30 A. Péter, K. Polgár and M. Tóth, *J. Cryst. Growth*, 2012, **346**, 69–74.
31 T. Koroleva, M. Kidibaev, A. Nehari, C. Pedrini, K. Lebbou, A. Belsky, A. Tcherepanov, A. Ishchenko, V. Ivanov, I. Sedunova, O. Teslenko, L. Viktorov, B. Shulgin, L. Zheng, J. Xu, V. Kononets and O. Sidletskiy, *Opt. Mater.*, 2013, **35**, 868–874.
32 J. B. Czirr, G. M. MacGillivray, R. R. MacGillivray and P. J. Seddon, *Nucl. Instrum. Methods Phys. Res., Sect. A*, 1999, **424**, 15.
33 B. Lire, C. Re, Y. Heng, R. Jia, Z. Fu, G. Ren, F. Yang, S. Pan, S. Li, X. Chen, S. Qian and G. Huang, *IEEE Nucl. Sci. Symp. Conf. Rec.*, 2011, 4627–4631.
34 T. Minami, *J. Non-Cryst. Solids*, 1985, **73**, 273–284.
35 M. I. Pantyukhina, G. V. Zelyutin, N. N. Batalov and V. P. Obrosov, *Russ. J. Electrochem.*, 2000, **36**, 792–795.
36 S. Ohta, S. Komagata, J. Seki, T. Saeki, S. Morishita and T. Asaoka, *J. Power Sources*, 2013, **238**, 53–56.
37 L. Jinlian, W. U. Xianming, C. Shang, C. Jianben and H. Zeqiang, *Bull. Mater. Sci.*, 2013, **36**, 687–691.
38 H. M. Rietveld, *J. Appl. Crystallogr.*, 1969, **2**, 65–71.
39 J. Rodríguez-Carvajal, *Phys. B*, 1993, **192**, 55–69.
40 R. Tycko, E. Schneider and A. Pines, *J. Chem. Phys.*, 1984, **81**, 680–688.
41 G. Kresse and J. Hafner, *Phys. Rev. B*, 1994, **49**, 14251–14271.
42 G. Kresse and J. Furthmüller, *Phys. Rev. B*, 1996, **54**, 11169–11186.
43 G. Kresse and D. Joubert, *Phys. Rev. B*, 1999, **59**, 1758–1775.
44 J. Perdew, A. Ruzsinszky, G. Csonka, O. Vydrov, G. Scuseria, L. Constantin, X. Zhou and K. Burke, *Phys. Rev. Lett.*, 2008, **100**, 136406.
45 G. Henkelman, B. P. Uberuaga and H. Jónsson, *J. Chem. Phys.*, 2000, **113**, 9901–9904.
46 V. Thangadurai, H. Kaack and W. J. F. Weppner, *J. Am. Ceram. Soc.*, 2003, **86**, 437–440.
47 R. J. Cava and E. A. Rietman, *Phys. Rev. B*, 1984, **30**, 6896–6902.
48 Z. Xu and J. F. Stebbins, *Solid State Nucl. Magn. Reson.*, 1995, **5**, 103–112.